Title

Development of high resolution 3D hyperpolarized carbon-13 MR molecular imaging techniques

Authors

Milshteyn, Eugene
von Morze, Cornelius
Reed, Galen D
et al.

Publication Date

2017-05-01

DOI

10.1016/j.mri.2017.01.003

Peer reviewed

HHS Public Access

Author manuscript

Magn Reson Imaging. Author manuscript; available in PMC 2018 May 01.

Published in final edited form as:

Magn Reson Imaging. 2017 May ; 38: 152–162. doi:10.1016/j.mri.2017.01.003.

Development of High Resolution 3D Hyperpolarized Carbon-13 MR Molecular Imaging Techniques

Eugene Milshteyn, B.S.[1,2], **Cornelius von Morze, Ph.D.**[1], **Galen D. Reed, Ph.D.**[3], **Hong Shang, Ph.D.**[1,2], **Peter J. Shin, Ph.D.**[1], **Zihan Zhu, B.S.**[1,2], **Hsin-Yu Chen, B.S.**[1,2], **Robert Bok, M.D., Ph.D.**[1], **Andrei Goga, M.D., Ph.D.**[4], **John Kurhanewicz, Ph.D.**[1,2], **Peder E. Z. Larson, Ph.D.**[1,2], and **Daniel B. Vigneron, Ph.D.**[1,2]

[1]Department of Radiology and Biomedical Imaging, University of California, San Francisco, California, USA

[2]UC Berkeley-UCSF Graduate Program in Bioengineering, University of California, San Francisco and University of California, Berkeley, California, USA

[3]HeartVista Inc., Los Altos, California, USA

[4]Department of Cell and Tissue Biology, University of California, San Francisco, California, USA

Abstract

The goal of this project was to develop and apply techniques for T_2 mapping and 3D high resolution (1.5 mm isotropic; 0.003 cm^3) ^{13}C imaging of hyperpolarized (HP) probes [1-^{13}C]lactate, [1-^{13}C]pyruvate, [2-^{13}C]pyruvate, and [^{13}C,$^{15}N_2$]urea in vivo. A specialized 2D bSSFP sequence was implemented on a clinical 3T scanner and used to obtain the first high resolution T_2 maps of these different hyperpolarized compounds in both rats and tumor-bearing mice. These maps were first used to optimize timings for highest SNR for single time-point 3D bSSFP acquisitions with a 1.5 mm isotropic spatial resolution of normal rats. This 3D acquisition approach was extended to serial dynamic imaging with 2-fold compressed sensing acceleration without changing spatial resolution. The T_2 mapping experiments yielded measurements of T_2 values of greater than 1 s for all compounds within rat kidneys/vasculature and TRAMP tumors, except for [2-^{13}C]pyruvate which was ~730 ms and ~320 ms, respectively. The high resolution 3D imaging enabled visualization the biodistribution of [1-^{13}C]lactate, [1-^{13}C]pyruvate, and [2-^{13}C]pyruvate within different kidney compartments as well as in the vasculature. While the mouse anatomy is smaller, the resolution was also sufficient to image the distribution of all compounds within kidney, vasculature, and tumor. The development of the specialized 3D sequence with compressed sensing provided improved structural and functional assessments at a high (0.003 cm^3) spatial and 2 s temporal resolution in vivo utilizing HP ^{13}C substrates by exploiting their long T_2 values. This 1.5 mm isotropic resolution is comparable to ^1H imaging and

Corresponding author: Daniel B. Vigneron, Department of Radiology and Biomedical Imaging, University of California, San Francisco, 1700 Fourth Street, Byers Hall Suite 102, San Francisco, CA 94158, dan.vigneron@ucsf.edu, Phone: 415-476-3343, Fax: 415-514-4451.

application of this approach could be extended to future studies of uptake, metabolism, and perfusion in cancer and other disease models and may ultimately be of value for clinical imaging.

Keywords

^{13}C; hyperpolarized; pyruvate; urea; DNP; SSFP

1. Introduction

Dissolution dynamic nuclear polarization (DNP) of carbon-13 enriched compounds with the aid of an electron paramagnetic agent and then rapidly dissolved, can increase the liquid state NMR signal-to-noise ratio (SNR) more than 10,000 fold [1]. MRI of hyperpolarized (HP) ^{13}C substrates is a powerful tool for detecting the metabolic and physiological changes that underlie disease processes in a noninvasive fashion [2–6]. However, the hyperpolarized signal is lost rapidly due to T_1 relaxation metabolic conversion, resulting in a limited temporal window for imaging. Furthermore, each applied radiofrequency pulse depletes the non-recoverable magnetization, creating design challenges for fast imaging approaches aimed at efficiently utilizing the hyperpolarized magnetization [1]. Therefore, specialized developments in MRI sequence design are required for hyperpolarized carbon-13 imaging. The implementation of different MRI data sampling strategies, including fast MRSI approaches such as echo-planar spectroscopic imaging with compressed sensing [7,8] and spiral MRSI [9], echo planar or spiral imaging with spectral-spatial excitation [10–14] and concentric rings trajectories [15], have all been applied in preclinical HP studies. While these sequences provided coverage and either sufficient spectral resolution (MRSI) or imaging of individual resonances (MRI), they were limited by relatively low spatial resolution, which can potentially limit their application.

The balanced steady-state free precession (bSSFP) sequence has the advantage of offering higher signal-to-noise ratios per unit time than other sequences [16,17]. This has been extensively demonstrated in proton imaging [18–20], and has consequently been utilized in HP ^{13}C imaging [21–25] for metabolic and perfusion imaging. As described previously [26], bSSFP sequences use the hyperpolarized magnetization effectively, exploiting the long relaxation times associated with various hyperpolarized probes. T_2 mapping can provide a valuable tool to measure the T_2 relaxation times of these probes in vivo and has been successfully performed with the bSSFP sequence with hyperpolarized urea [22], thereby allowing proper optimization of subsequent imaging acquisitions for the specific T_2 values.

Hyperpolarized ^{13}C pyruvate MRI studies have demonstrated several potential applications including cancer [2], diabetes [27], and cardiac disease [13,28]. The hyperpolarized lactate-to-pyruvate ratio reflects changes in glycolysis related to the enzyme lactate dehydrogenase (LDH) that is up-regulated in human cancers including prostate [2,4,29,30]. Measurements of LDH kinetics by HP ^{13}C-pyruvate MR have shown significant differences between cancer and normal tissues and with therapeutic response in preclinical models [31–34]. The feasibility and safety of HP ^{13}C-pyruvate MRI was demonstrated in a Phase 1 clinical trial of 31 prostate cancer patients [3]. Also, recent studies incorporating new sequence

development have shown the utility of this MR molecular imaging technique to probe not only metabolism, but also perfusion and vascular permeability [35–38]. Additionally, recent studies of tumor pathogenesis have focused on the heterogeneous nature of tumors, based on the hypothesis that subpopulations of tumor cells may drive proliferation and aggressiveness of the disease, specifically as regards to the concepts of lactate shuttling and the "reverse Warburg effect," suggesting the importance of lactate as a probe for metabolism [29]. The spatial heterogeneity of tumor metabolism and perfusion is not readily measured by current clinical methods, but may have considerable diagnostic and predictive value, such as in assessing aggressiveness and guiding biopsies [39,40]. HP [^{13}C]urea has been applied to image tumor perfusion [35], and can be readily combined with metabolic probes to simultaneously assess changes in both metabolism and perfusion [36] and has also been recently applied for cardiac perfusion imaging [38]. Urea is also important in renal function and renal urea handling can be measured using hyperpolarized MRI [22,37]. Hyperpolarized urea furthermore has an exceptional safety profile as a medical imaging contrast agent.

The goal of this study was to investigate a new approach for tissue characterization using high resolution HP MR imaging of [1-^{13}C]pyruvate, [2-^{13}C]pyruvate, [1-^{13}C]lactate, and [^{13}C,$^{15}N_2$]urea in vivo in both normal rats and tumor-bearing mice at 3 Tesla. T_2 mapping with a 2D bSSFP sequence allowed identification of the distribution of T_2 values of each compound in different biological compartments in vivo at a high in-plane resolution. A custom 3D bSSFP sequence was then applied for high resolution imaging of each compound, including both single time-point and serial dynamic images. This was performed with the incorporation of compressed sensing as well as using parameters derived from the T_2 mapping results. In this project, the biodistribution and temporal dynamics of the injected HP compounds was investigated with 1.5 mm isotropic resolution within rat and mouse kidneys and vasculature as well as in tumors from transgenic mouse models of cancer.

2. Methods

2.1 Hyperpolarization

Neat [1-^{13}C]pyruvic acid (Sigma Aldrich, St. Louis, MO, USA) was mixed with 15 mM trityl radical (GE Healthcare, Waukesha, WI) and 1.5 mM Gd-DOTA (Guerbet, Roissy, France). Neat [2-^{13}C]pyruvic acid (Sigma Aldrich) was mixed with 15 mM trityl radical (GE Healthcare, Waukesha, WI) and 1.5 mM Gd-DOTA. Neat [1-^{13}C]lactic acid (Sigma Aldrich) was mixed with a small amount of distilled water for liquification and mixed with 15 mM trityl radical OX063 (Oxford Instruments, Abingdon, UK) and 1 mM Gd-DOTA. [^{13}C,$^{15}N_2$]Urea (Sigma Aldrich) was dissolved in glycerol and mixed with 15 mM trityl radical OX063 (Oxford Instruments, Abingdon, UK) and 1.5 mM Gd-DOTA. Each compound was individually polarized in either a HyperSense dissolution DNP system (Oxford Instruments, Abingdon, UK) operating at 1.35 K and 3.35 T (lactic acid [41] and urea [22]) for ~1hr or a SpinLab (GE Healthcare, Waukesha, WI), operating at 0.8K and 3.35T (pyruvic acids [42]) for ~2hrs to achieve polarizations of 20–25% (urea and lactate) to 30–35% (pyruvic acids). The dissolution media and resulting concentration for each compound was as follows: 4.5 mL of 80 mM NaOH/40 mM Tris buffer for [1-^{13}C]pyruvic acid resulting in 80 mM [1-^{13}C]pyruvate (hereafter referred to as C_1-pyruvate); 4.5 mL of 80

mM NaOH/40 mM Tris buffer for [2-^{13}C]pyruvic acid resulting in 80 mM [2-^{13}C]pyruvate (hereafter referred to as C_2-pyruvate); 4.5 mL of 160 mM NaOH/40 mM Tris buffer for [1-^{13}C]lactic acid resulting in 160 mM [1-^{13}C]lactate (hereafter referred to as lactate); 5mL of 1x phosphate-buffered saline for [^{13}C,$^{15}N_2$]urea resulting in 110 mM [^{13}C,$^{15}N_2$]urea (hereafter referred to as urea).

2.2 Animal Handling

All animal studies were done under protocols approved by the University of California San Francisco Institutional Animal Care and Use Committee (IACUC). Six normal Sprague-Dawley rats (three for T_2 mapping, three for 3D imaging), six transgenic adenocarcinoma of mouse prostate (TRAMP) mice [43], and one oncogene-driven breast cancer mouse [44] were used in these studies. Both the rats and mice were anesthetized with isoflurane (1.5%) and placed in a supine position on a heated pad throughout the duration of the experiments. After polarization and dissolution, each of the compounds were injected into the animal via tail vein catheters: ~3 mL over 12 s for each rat and ~500 μL over 15 s for each mouse.

2.3 Image Acquisition and Reconstruction

All experiments were performed on a 3T GE MR750 clinical scanner (GE Healthcare, Waukesha, WI) with multinuclear capability. The studies were performed with dual-tuned ^{1}H/^{13}C transceiver birdcage radiofrequency coils that have either a diameter of 8 cm for rats or a diameter of 5 cm for mice [31].

All acquisitions were performed using a custom ^{13}C bSSFP sequence with either one phase encoding dimension (projection along the anterior-posterior direction) (T_2 Mapping) or two (3D imaging) phase encoding dimensions. In each acquisition, a flip angle of 180 degrees was used for optimized SNR, off-resonance insensitivity, and near optimal k-space filtering effect [17]. $\alpha/2$ – TR/2 preparation pulses were used to reduce transient state signal oscillations [26]. A basic sinc RF pulse was used for both the 90° preparatory pulse and 180° pulses train with linear scaling (3.2 ms pulse duration, TBW = 4 for T_2 mapping and 1.6 ms pulse duration, TBW = 4 for 3D imaging). A 1mL enriched [^{13}C]urea vial phantom (6.0M) was used for frequency and power calibration. For anatomical localization, 3D bSSFP proton (16 × 8 × 4.8 cm, 256 × 128 × 80, 5.1 ms TR, 50° flip angle) images were obtained for rat studies, while T_2-weighted fast spin echo proton (6 × 6 × 8 cm, 256 × 192 × 40, 7.6 s TR) images were obtained for mouse studies. The acquisitions were started at 30 s after injection for T_2 mapping and 20 s for all 3D imaging.

The T_2 mapping for C_1-pyruvate and lactate in rat kidneys (Figure 1 and Figure 3), as well as pyruvate, lactate, and urea in mouse tumors (Figure 1 and Figure 4) were acquired similarly to prior studies for [^{13}C,$^{15}N_2$]urea [22]. Briefly, the parameters were 14 × 7 cm FOV, 140 × 70 matrix size yielding 1 mm in-plane resolution for the coronal acquisitions, 11 ms TR, 770 ms temporal resolution, 15.4 s total scan time for 20 dynamic images, each acquired in projection mode. The parameters for TRAMP T_2 mapping were 3 × 3 cm FOV, 30 × 30 matrix size yielding 1 mm in-plane resolution for the coronal acquisitions, 11 ms TR, 330 ms temporal resolution, 6.6 s total scan time for 20 dynamic images. C_2-pyruvate T_2 maps were acquired with a coarser resolution due to SNR considerations, specifically a

14 × 7 cm FOV, 56 × 28 matrix size yielding 2.5 mm in-plane resolution (rat) or 8 × 4 cm FOV, 36 × 18 matrix size yielding ~2 mm in-plane resolution (TRAMP mouse) for the coronal acquisitions, while keeping the other parameters the same. The T_2 maps were reconstructed using a nonnegative least squares algorithm with Tikhonov regularization as described in [45]. Briefly, pseudo-spectra were generated with the algorithm based on an input of 128 logarithmically-spaced T_2 values and an exponential decay model, and the long (>2 s) and short (<2 s) T_2 components [22] and associated amplitudes were found based on the peaks in the pseudo-spectra. An SNR cutoff based on the first time point was used to determine which pixels would be fit for each of the compounds: 30 for lactate in rat kidney, 15 for C_1-pyruvate in rat kidney, 20 for C_2-pyruvate in rat kidney, and 15 for all compounds in mouse tumor. As an example of the T_2 mapping acquisition, Figure 1 depicts the full dynamic set of images for acquisition of lactate in a rat (a) and mouse tumor (b). Associated bilinear (semilog plot) and biexponential decay for a single pixel in rat kidney, and linear (semilog plot) and monoexponential decay for a single pixel in mouse tumor are also provided.

Since the contribution of signal from metabolic products of lactate [41] and C_2-pyruvate [46] is negligible in comparison with the primary injected substrate, for the acquisitions as described, the measured T_2's should represent the true T_2's of these substrates. In the case of C_1-pyruvate, however, the measurements reflect an aggregate T_2 of C_1-pyruvate and its metabolic products lactate and alanine.

The 3D fully sampled rat acquisitions (Figure 5) had the following parameters: 12 × 6 × 2.4 cm^3 FOV extending throughout the heart and abdomen, 80 × 40 × 12 matrix size, yielding a 1.5 mm isotropic spatial resolution (0.003 cm^3), 8.5 ms/4.25 ms TR/TE for a total scan time of ~4 s. A Cartesian raster encoding scheme was used, giving a ~2 s effective echo time. SNR was calculated in MATLAB by manually drawing ROIs in kidney and vasculature slices with the highest signal, as well as a region containing only noise. C_2-pyruvate 3D imaging in the rat was performed using partial Fourier encoding along one phase encoding dimension, acquiring only 5/6 of k-space, while keeping other parameters the same as previously mentioned. The data were reconstructed using a projection onto convex sets (POCS) reconstruction [47,48]. The 3D fully sampled mouse cancer model acquisitions (Figure 6) had the following parameters: 6.4 × 4.8 × 1.6 cm^3 FOV, 32 × 24 × 8 matrix size, yielding a 2 mm isotropic spatial resolution (0.008 cm^3). An 8.5 ms TR for a total scan time of ~1.6 s was still used. The Cartesian raster encoding scheme gave a ~0.8 s effective echo time. The resulting carbon images were interpolated to 256 × 256 in-plane and either aligned with (rats) or overlaid onto (mice) proton images in multiple orientations using Osirix [49].

The TRAMP cancer model acquisition (Figure 7) was then modified to use compressed sensing for higher temporal resolution allowing for 3D high resolution dynamic imaging. A variable-density pattern, designed with a Monte-Carlo simulation [50] and shown in Figure 2a, was chosen to accelerate the acquisition two-fold with fully acquire k-space center, while maintaining the same 1.5 mm nominal spatial resolution. The parameters for each acquisition were 3 × 3 × 2.55 cm^3 FOV, 20 × 20 × 17 matrix size, 8.5 ms TR for a total acquisition time of ~1.4 s per dynamic time point. A 600 ms delay was used between successive time points, giving a total acquisition time of ~20 s for 10 dynamic 3D

acquisitions. The resulting data was reconstructed using a ℓ_1-penalized nonlinear conjugate gradient algorithm with a Daubeches-4 wavelet transform on each individual time point, similar to the reconstructions described in [50]. This algorithm was used to solve the following problem:

$$argmin_m \|F_u m - y\|_2 + \lambda \|\psi m\|_1 + \alpha TV_x(m)$$

where m is the reconstructed MRI image, F_u is the undersampled Fourier Transform operator associated with the sampling pattern, y is the acquired data, ψ is the sparsifying transform, λ is the weight for ℓ_1-norm minimization, TV_x is the total variation (TV) penalty for the spatial dimensions, and α is the weight for the TV penalty. The λ and α parameters were chosen empirically to be 0.005 and 0.00005, respectively, via retrospective simulations of 50% undersampling of a previously acquired fully sampled dataset. Figure 2b depicts the results of the simulation with a comparison of a representative tumor slice. The reconstructed image matches the original image very closely based on the difference image, which was scaled up by a factor of 5 for visualization. The structural similarity index (SSIM) and normalized root mean squared error (NRMSE) were calculated to quantify these differences, which resulted in a SSIM value of 0.9255 and NRMSE of 7.00%, indicating the pattern design and undersampling factor were suitable for high resolution dynamic imaging.

3. Results

3.1 T_2 Mapping

The mean T_2 distribution of lactate, C_1-pyruvate, and C_2-pyruvate can be seen in both Figure 3a and Table 1, where a decrease in T_2 was observed from the vasculature to the renal cortex. The longest mean T_2 values of lactate, at ~2.6 s, were measured in the vasculature, with a decrease to ~1.95 s in the kidneys. Decreasing values were observed from the renal pelvis to the renal cortex. A similar trend was observed with C_1-pyruvate, albeit with about 30% lower values as compared to lactate, and C_2-pyruvate, with a mean T_2 value of ~0.75 s in both vasculature and kidney. Figure 3b and 3c show the long and short T_2 components, respectively, of each compound. The short T_2 component was evident in both vasculature and kidney among all compounds, while lactate showed considerable long components, especially in the vasculature. Previously acquired T_2 maps of urea show a similar distribution within the kidney [22], and the results presented here are relatively similar to the results of previous T_2 measurements of these ^{13}C compounds [51,52]. Though the lactate and C_1-pyruvate experiments yielded T_2 values of approximately half those of urea [22], these values were still long enough to be exploited effectively for high resolution imaging since the T_1 and T_2 were either longer or on the order of the effective echo time of the subsequent 3D experiments, allowing for acquisition of high k-space signal with rasterized phase encoding and insignificant T_2 blurring [26].

Within the TRAMP tumor, the mean T_2 measurements (Figure 4) for lactate, C_1-pyruvate, and urea ranged from ~1.8–2.5 s, while C_2-pyruvate was ~0.3 s, similar to previous studies [51,52]. The tumors had some T_2 variability with the intra-tumor standard deviation equaling ~10–20% of the mean value due to the inherent spatial heterogeneity in these

tumors. Similar to the T_2 mapping for rat kidneys and vasculature, the T_2 values were still long enough to be utilized for high spatial resolution imaging for both single time point and serial dynamic imaging with the bSSFP sequence. The effective echo times were also relatively short compared to T_1 and T_2 due to the fewer phase encodes acquired for single time point (smaller FOV compared to rat) and serial dynamic imaging (smaller FOV and undersampling).

3.2 Fully Sampled 3D Rat and Mouse Cancer Model Imaging

Figure 5 shows the resulting 3D images in rats of lactate, C_1-pyruvate, and C_2-pyruvate. Uptake and biodistribution of these compounds can be seen within the kidney, with the image resolution being sufficient to visualize the renal pelvis and cortex of the kidney, as well as the connecting vasculature components. Figure 5a features all 12 slices corresponding to the 3D lactate acquisition, with the SNR being high enough to also visualize signal in the heart. Figure 5b features representative slices of lactate and C_1-pyruvate next to the corresponding ^{1}H image, as well as the reformatted axial slices, owing to the 3D isotropic nature of the acquisition. Figure 5c shows a representative C_2-pyruvate slice overlaid onto the corresponding ^{1}H image. The SNR trend between these three compounds followed the mean T_2 trend discussed previously. However, the SNR of C_2-pyruvate was still high enough at 1.5 mm isotropic resolution to see uptake in the vasculature and kidneys. The resulting SNR within different parts of the rat kidney, as well as the vasculature, is presented in Table 2.

Similarly, the 3D images of the TRAMP and breast cancer mice in Figure 6 overlaid on top of the ^{1}H images, show uptake of C_1-pyruvate within the kidneys and the tumor. While the mouse anatomy is smaller, the resolution here was also sufficient to image the distribution of C_1-pyruvate within vasculature, renal pelvis and cortex, and tumor. With the effective echo time being only ~2 s for rat acquisitions and ~1.4 s for mice acquisitions, the long T_2 values of these molecular probes enabled sufficient SNR with the bSSFP sequence to obtain 1.5 mm and 2 mm isotropic resolution, respectively, for the depiction of these anatomical structures.

3.3 Compressed Sensing TRAMP Imaging

The 2x fold acceleration via compressed sensing was shown to successfully acquire dynamic data of hyperpolarized C_1- and C_2-pyruvate, lactate, and urea while improving the spatial resolution utilized in the previously shown fully sampled data by 25% in each spatial dimension. There was no observed SNR loss with the compressed sensing acquisition even with a higher spatial resolution as evidenced by 2x fold SNR difference between the first dynamic time point and the fully sampled acquisition (~40 vs. ~20) of C_1-pyruvate. The first five time-points of the 3D dynamic acquisition from a representative kidney and tumor slice are shown in Figure 7a–c, with C_2-pyruvate carbon images overlaid on top of ^{1}H images in 7d (tumor) and 7e (tumor). With the 1.5 mm isotropic resolution, uptake and distribution of all three compounds within kidneys, vasculature, and tumor was seen, similar to the fully sampled images above. Furthermore, the differences in the dynamics of each compound correlated with the mean T_2 values mentioned previously, whereby C_2-pyruvate quickly decayed due to both relaxation and metabolism, while lactate and urea persisted longer,

especially in the kidney, owing to the long T_2 values mentioned here and measured previously. While not shown here, injection of C_1-pyruvate instead of C_2-pyruvate yielded similar results as with C_2-pyruvate, albeit the dynamic signal lasted slightly longer due to the longer T_1 and mean T_2 value.

4. Discussion

The results of this study demonstrated the feasibility and capability of 1.5 mm isotropic resolution hyperpolarized carbon-13 imaging on a 3T clinical scanner with the bSSFP sequence. Metabolically important compounds, such as pyruvate and lactate, as well as a perfusion agent, urea, were imaged at high enough spatial resolution to determine distribution, uptake, and structural morphology within specific anatomical features, such as different kidney compartments and inhomogeneity within tumors. 1 mm in-plane T_2 maps were also generated, showing the existence of long and short components for the different compounds, both corroborating previous studies on the in vivo carbon-13 T_2's, as well as providing a better anatomical distribution of the T_2's. The feasibility of using compressed sensing in conjunction with the bSSFP sequence was demonstrated for improved temporal resolution without sacrificing spatial resolution, which may be useful for translating this approach for clinical imaging, as larger volume coverage (larger matrix sizes) will necessitate increased sequence acceleration.

The T_2 values of pyruvate (C_1 and C_2) and lactate identified within rat kidneys and vasculature can be explained based on the relaxation mechanisms associated with ^{13}C labeled compounds such as chemical shift anisotropy and the dipolar relaxation [22,53,54]. The relative contribution of each of these pathways remains unknown in vivo, as is the net contribution from intra- and intermolecular relaxation pathways and relaxation from transport between differing microenvironments. Furthermore, T_1 and inflow can have an effect on T_2 calculation, as described previously [22].

With C_1-pyruvate and lactate exhibiting >~1 s short and long components, this may indicate relatively free rotation and diffusion within both vasculature and kidneys, leading to shorter rotational correlation times and longer T_2 values. The presence of monocarboxylate transporters (MCTs) in red blood cells indicate each compound can be transported into and out of the cells [55–57] and would subsequently not be hindered in free movement about the vasculature or within different kidney compartments [58]. Furthermore, paramagnetic effects arising from certain oxidation states of hemoglobin may also have a significant relaxation effect on molecules that are transported into RBCs. The longer T_2 values within the renal pelvis compared to the renal cortex and medulla can potentially be attributed to the presence of glomerular filtrate, which is free from red blood cells [22], leading to a longer solution-like T_2. There is lower lactate dehydrogenase (LDH) activity in both renal pelvis and vasculature as well [59], leading to less metabolic conversion to shorter T_2 compounds, and a higher calculated T_2. This reasoning can also be applied to explain the differences in T_2 between each of the compounds, with lactate less readily back-converted to pyruvate via LDH and thus having the longest measured T_2, while conversely C_2-pyruvate is more readily converted to either C_2-lactate or other compounds in the citric acid cycle, which leads to a shorter measured T_2 due to the contributions of these shorter T_2 compounds, with C_1-

pyruvate being somewhere in the middle. Furthermore, C_2-pyruvate has a much shorter initial relaxation time because of the dipolar relaxation term since a proton is one bond closer to the ^{13}C of the compound compared to C_1-pyruvate and lactate. This point was corroborated by performing a T_2 measurement on hyperpolarized aqueous C_1- and C_2-pyruvate via a CPMG sequence with a TR of 10 ms. The measured T_2 of C_2-pyruvate (21 ± 2.9 s) was ~84% of C_1-pyruvate (25 ± 0.7 s), indicating the effect of dipolar relaxation. The role of dipolar and chemical shift anisotropy relaxation, as well as potential paramagnetic relaxation [54] in the vicinity of hemoglobin, needs to be studied further to get a full understanding of the in vivo T_2 distribution, specifically the relaxation properties of each compound, such as, for example, the enhanced role of the dipolar relaxation in the conversion of C_2-pyruvate to C_2-lactate, as well as the potential differences when the compounds are intracellular versus extracellular. Further progress in the development of long-lived hyperpolarized ^{13}C probes, such as the chemical design of the probes and extension of hyperpolarized lifetimes, can help identify the relaxation mechanisms governing a compound's in vivo T_1 and T_2 [60,61].

The 3D high resolution imaging of the rat kidney agreed with the T_2 mapping, with the highest SNR being within the vasculature and renal pelvis, and lactate having the highest SNR and C_2-pyruvate having the lowest. Additionally, SNR was sufficient at 1.5 mm isotropic resolution from the heart to visualize uptake of lactate and pyruvate. Within the kidney, the biodistribution of each compound correlated with previous metabolic studies, with an infusion of either pyruvate or lactate resulting in stronger signal from the cortex and renal pelvis compared to the medulla [58,62]. In normal kidney function, especially after infusion, both lactate and pyruvate are readily metabolized, with reduction of pyruvate to lactate and oxidation of lactate to pyruvate, as well as conversion of lactate to glucose via gluconeogenesis and conversion to amino acids. Lactate and pyruvate can also be reabsorbed by the proximal tubule. These processes occur primarily in the cortex, correlating with the uptake and biodistribution seen in the 3D imaging.

Compared to the rat kidneys, the T_2 distribution and subsequent 3D imaging of the TRAMP tumors was more varied in terms of uptake and biodistribution, a consequence of tumor heterogeneity [63]. The relaxation mechanisms previously discussed can also be applied within the tumor environment, including the role of metabolism, since LDH activity is relatively much higher within tumors compared to normal tissue, and vascularity, with the presence of leaky blood vessels allowing for relatively free rotation and shorter rotational correlation times [29,51]. Exchange between intracellular and extracellular pools within the tumor can cause T_2 shortening, potentially due to short T_2 components coming from the intracellular pool [64]. While C_2-pyruvate clearly had the shortest mean T_2 value, the other three compounds all had similar T_2 values, and all four compounds had moderate intratumoral standard deviations, potentially indicating some spatial heterogeneity within the TRAMP tumors, which was similarly seen with injected [1-^{13}C]pyruvate in an earlier study [65]. This can be attributed to the presence of microenvironments and several competing mechanisms that affect the infused compounds, such as MCT and LDH activity, lactate shuttling, reverse Warburg effect, and tumor hypoxia [40,66,67]. These effects also extend to the 3D dynamic imaging, whereby the spatial biodistribution of the compounds, and

consequent signal decay, can be attributed to the different mechanisms governing metabolism and perfusion within the tumor.

The use of C_2-pyruvate in this study is potentially useful for looking at tumor metabolism with the bSSFP sequence without sacrificing the SNR and spatial resolution advantages. Previously, C_2-pyruvate has been extensively used to study the Krebs cycle, especially within the context of cardiac metabolism [9,68,69]. While the C_1-pyruvate T_2 mapping and 3D imaging in this study include significant contributions from its metabolites lactate, alanine, and pyruvate-hydrate due to the close resonances of all these compounds at 3 Tesla (not an issue after injection of [1-^{13}C]lactate due to much smaller metabolic conversion [41]), the C_2 labeled versions of these metabolites arising from the metabolic conversion of C_2-pyruvate resonate 100+ ppm away from C_2-pyruvate [70]. Therefore, with the 1.6 ms sinc RF pulse (excitation bandwidth of 2500 Hz) used in this study, the signal arising from any C_2-metabolites are negligible compared to the C_2-pyruvate, and the resulting images (in the case of rat kidney) and signal decay (in the case of TRAMP tumors) reflect more accurately the effects on C_2-pyruvate in the specific microenvironment.

In general, single metabolite imaging of hyperpolarized ^{13}C compounds can provide a high resolution view of the biodistribution and uptake of said compounds in a very fast and efficient manner. When dealing with a single frequency system, as is the case for C_2-pyruvate, [^{13}C,$^{15}N_2$]urea, and C_1-lactate in this study, pulse design becomes much easier and much shorter TRs are achievable, allowing for high resolution imaging, as was demonstrated in this study. Urea, as a metabolically-inactive compound, can provide perfusion information and thus has a direct application as a single injected hyperpolarized compound. However, metabolically active compounds, such as C_2-pyruvate and C_1-lactate, can provide additional information due to their cellular uptake and metabolism. The utility in imaging these single metabolites after injection may be similar to the information obtained from positron emission tomography (PET) imaging, such as standard uptake values or fitting the dynamics to a pharmokinetic model. Compared to PET, hyperpolarized ^{13}C imaging can be much faster and without radiation exposure, while still reporting on uptake of metabolically active compounds [2]. In addition, hyperpolarized ^{13}C has advantages over other perfusion MRI techniques, such as gadolinium-based approaches and arterial spin labeling, including signal to tracer concentration proportionality, high SNR and CNR, no gadolinium toxicity issues, and the capability of simultaneously injecting multiple probes [35,37,71].

Imaging of C_1-pyruvate and/or the resulting C_1 metabolites with the bSSFP sequence would necessitate either the use of suppression pulses, which can be challenging with such close resonances at 3 Tesla, or long excitation/refocusing pulses, which would offset some of the advantages of the bSSFP sequence. Recently, C_1-pyruvate and produced C_1-lactate were imaged on a 14T system using a specially designed multiband spectrally selective pulse and an appropriate choice of TR [72]. This approach could, in principle, be applied on a 3T clinical scanner, although trade-offs would need to be made between spatial and temporal resolution.

The ability to obtain 3D 1.5 mm isotropic images for ^{13}C can be very advantageous for assessment of disease within specific organs, especially at the clinically relevant field strength of 3 Tesla. Current acceptable parameters for proton imaging of prostate cancer features slice thicknesses of ~3 mm and in-plane resolution of ≤2 mm for various acquisitions, such as dynamic contrast enhanced MRI [73–75]. Furthermore, 3D isotropic imaging is most desirable due to the ability to limit patient scanning, while simultaneously acquiring all the desired information in all three planes [76]. Recently, work by Nielsen et al. [77] and Bertelsen et al. [78] demonstrated 1.25 mm isotropic resolution imaging of [^{13}C,$^{15}N_2$]urea with a 3D bSSFP sequence in rat kidneys on a 9.4T preclinical scanner with higher performance gradients enabling shorter achievable TRs. This allowed high spatial resolutions to be achieved. By comparison, our initial rat kidney results featured slightly lower 1.5 mm isotropic resolution, but utilized clinical gradient strengths and shorter T_2 compounds. Nevertheless, both sets of results demonstrate the feasibility of obtaining approximately 1 mm isotropic resolution for hyperpolarized ^{13}C compounds, especially on 3T clinical scanners, as was recently demonstrated in [45]. Recent work on [^{13}C,$^{15}N_2$]urea imaging on pigs at 3T [79] shows feasibility of imaging larger animals, although at a considerably coarser spatial resolution.

The sequence presented here could potentially be further optimized for improved dynamic imaging by employing both newer undersampling reconstruction strategies, such as a wavelet along time or low rank plus sparse approach [8,80]. A variable flip angle scheme can be implemented for each desired metabolite using a non-convex optimization approach that would increase SNR, reduce image blurring, and improve off-resonance insensitivity for single time-point images, or maximize SNR for high resolution dynamic imaging [81]. The bSSFP sequence and these specific acquisition and reconstruction approaches can also be readily combined with parallel imaging [82,83], which may be required as the translation from preclinical to clinical imaging will require larger matrix sizes for the same desired isotropic resolution.

5. Conclusion

In this study we performed high resolution HP ^{13}C imaging using the bSSFP sequence. T_2 mapping was performed on rat kidneys and vasculature, as well as tumor-bearing mice, using [1-^{13}C]pyruvate, [1-^{13}C]lactate, [2-^{13}C]pyruvate, and [^{13}C,$^{15}N_2$]urea. We tailored the bSSFP acquisition to the measured T_2's to obtain 1.5 mm isotropic single time-point images of biodistribution within rat kidneys and vasculature in only ~4 s. Using 2-fold compressed sensing acceleration, we extended the high resolution single-time-point imaging framework to dynamic imaging without having to sacrifice spatial resolution, enabling us to obtain biodistribution data at 1.5 mm isotropic resolution every 2 s. The HP ^{13}C methods presented here can be utilized for high resolution dynamic imaging of metabolism, biodistribution, and perfusion.

Acknowledgments

We gratefully acknowledge grant support from NIH P41EB013598, R01EB013427, R01EB017449, R01CA166655 and R01CA170447. NIH K01DK099451 supported CVM.

References

1. Ardenkjaer-Larsen JH, Fridlund B, Gram A, Hansson G, Hansson L, Lerche MH, et al. Increase in signal-to-noise ratio of > 10,000 times in liquid-state NMR. Proc Natl Acad Sci U S A. 2003; 100:10158–63. DOI: 10.1073/pnas.1733835100 [PubMed: 12930897]
2. Kurhanewicz J, Vigneron DB, Brindle K, Chekmenev EY, Comment A, Cunningham CH, et al. Analysis of cancer metabolism by imaging hyperpolarized nuclei: prospects for translation to clinical research. Neoplasia. 2011; 13:81–97. DOI: 10.1593/neo.101102 [PubMed: 21403835]
3. Nelson SJ, Kurhanewicz J, Vigneron DB, Larson PEZ, Harzstark AL, Ferrone M, et al. Metabolic imaging of patients with prostate cancer using hyperpolarized [1-^{13}C]pyruvate. Sci Transl Med. 2013; 5:198ra108.doi: 10.1126/scitranslmed.3006070
4. Wilson DM, Kurhanewicz J. Hyperpolarized ^{13}C MR for Molecular Imaging of Prostate Cancer. J Nucl Med. 2014; 55:1567–72. DOI: 10.2967/jnumed.114.141705 [PubMed: 25168625]
5. Comment A, Merritt ME. Hyperpolarized Magnetic Resonance as a Sensitive Detector of Metabolic Function. Biochemistry. 2014; 53:7333–57. DOI: 10.1021/bi501225t [PubMed: 25369537]
6. Brindle KM, Bohndiek SE, Gallagher FA, Kettunen MI. Tumor Imaging Using Hyperpolarized Resonance Spectroscopy ^{13}C Magnetic. Magn Reson Med. 2011; 66:505–19. DOI: 10.1002/mrm.22999 [PubMed: 21661043]
7. Larson PEZ, Bok R, Kerr AB, Lustig M, Hu S, Chen AP, et al. Investigation of tumor hyperpolarized [1-^{13}C]-pyruvate dynamics using time-resolved multiband RF excitation echo-planar MRSI. Magn Reson Med. 2010; 63:582–91. DOI: 10.1002/mrm.22264 [PubMed: 20187172]
8. Larson PEZ, Hu S, Lustig M, Kerr AB, Nelson SJ, Kurhanewicz J, et al. Fast Dynamic 3D MRSI with Compressed Sensing and Multiband Excitation Pulses for Hyperpolarized ^{13}C Studies. Magn Reson Med. 2011; 65:610–9. DOI: 10.1016/j.biotechadv.2011.08.021.Secreted [PubMed: 20939089]
9. Park JM, Josan S, Jang T, Merchant M, Watkins R, Hurd RE, et al. Volumetric spiral chemical shift imaging of hyperpolarized [2-^{13}C]pyruvate in a rat c6 glioma model. Magn Reson Med. 2015; doi: 10.1002/mrm.25766
10. Lau AZ, Chen AP, Ghugre NR, Ramanan V, Lam WW, Connelly KA, et al. Rapid multislice imaging of hyperpolarized ^{13}C pyruvate and bicarbonate in the heart. Magn Reson Med. 2010; 64:1323–31. DOI: 10.1002/mrm.22525 [PubMed: 20574989]
11. Cunningham CH, Chen AP, Lustig M, Hargreaves BA, Lupo J, Xu D, et al. Pulse sequence for dynamic volumetric imaging of hyperpolarized metabolic products. J Magn Reson. 2008; 193:139–46. DOI: 10.1016/j.jmr.2008.03.012 [PubMed: 18424203]
12. Reed GD, Larson PEZ, Von Morze C, Bok R, Lustig M, Kerr AB, et al. A method for simultaneous echo planar imaging of hyperpolarized ^{13}C pyruvate and ^{13}C lactate. J Magn Reson. 2012; 217:41–7. DOI: 10.1016/j.jmr.2012.02.008 [PubMed: 22405760]
13. Miller JJ, Lau AZ, Teh I, Schneider JE, Kinchesh P, Smart S, et al. Robust and high resolution hyperpolarized metabolic imaging of the rat heart at 7 T with 3D spectral-spatial EPI. Magn Reson Med. 2015; doi: 10.1002/mrm.25730
14. Gordon JW, Vigneron DB, Larson PEZ. Development of a Symmetric Echo Planar Imaging Framework for Clinical Translation of Rapid Dynamic Hyperpolarized ^{13}C Imaging. Magn Reson Med. 2016; :1–7. DOI: 10.1002/mrm.26123
15. Jiang W, Lustig M, Larson PEZ. Concentric rings K-space trajectory for hyperpolarized ^{13}C MR spectroscopic imaging. Magn Reson Med. 2016; 75:19–31. DOI: 10.1002/mrm.25577 [PubMed: 25533653]
16. Scheffler K, Lehnhardt S. Principles and applications of balanced SSFP techniques. Eur Radiol. 2003; 13:2409–18. DOI: 10.1007/s00330-003-1957-x [PubMed: 12928954]
17. Bieri O, Scheffler K. Fundamentals of balanced steady state free precession MRI. J Magn Reson Imaging. 2013; 38:2–11. DOI: 10.1002/jmri.24163 [PubMed: 23633246]
18. Çukur T. Spectrally selective imaging with wideband balanced steady-state free precession MRI. Magn Reson Med. 2015; doi: 10.1002/mrm.25700
19. Krishnamurthy R, Pednekar A, Atweh LA, Vogelius E, Chu ZD, Zhang W, et al. Clinical validation of free breathing respiratory triggered retrospectively cardiac gated cine balanced steady-state free

precession cardiovascular magnetic resonance in sedated children. J Cardiovasc Magn Reson. 2015; 17:1.doi: 10.1186/s12968-014-0101-1 [PubMed: 25589308]

20. Quist B, Hargreaves BA, Daniel BL, Saranathan M. Balanced SSFP Dixon imaging with banding-artifact reduction at 3 Tesla. Magn Reson Med. 2015; 74:706–15. DOI: 10.1002/mrm.25449 [PubMed: 25227766]
21. Månsson S, Petersson JS, Scheffler K. Fast metabolite mapping in the pig heart after injection of hyperpolarized ^{13}C-pyruvate with low-flip angle balanced steady-state free precession imaging. Magn Reson Med. 2012; 68:1894–9. DOI: 10.1002/mrm.24183 [PubMed: 22294528]
22. Reed GD, Von Morze C, Bok R, Koelsch BL, Van Criekinge M, Smith KJ, et al. High Resolution ^{13}C MRI With Hyperpolarized Urea: In Vivo T_2 Mapping and ^{15}N Labeling Effects. IEEE Trans Med Imaging. 2014; 33:362–71. [PubMed: 24235273]
23. Von Morze C, Sukumar S, Reed GD, Larson PEZ, Bok RA, Kurhanewicz J, et al. Frequency-specific SSFP for hyperpolarized ^{13}C metabolic imaging at 14. 1 T. Magn Reson Imaging. 2013; 31:163–70. DOI: 10.1016/j.mri.2012.06.037 [PubMed: 22898680]
24. Leupold J, Månsson S, Stefan Petersson J, Hennig J, Wieben O. Fast multiecho balanced SSFP metabolite mapping of ^{1}H and hyperpolarized ^{13}C compounds. Magn Reson Mater Physics, Biol Med. 2009; 22:251–6. DOI: 10.1007/s10334-009-0169-z
25. Bhattacharya P, Harris K, Lin A, Mansson M, Norton V, Perman W, et al. Ultra-fast three dimensional imaging of hyperpolarized ^{13}C in vivo. MAGMA. 2005; 18:245–56. [PubMed: 16320090]
26. Svensson J, Månsson S, Johansson E, Petersson JS, Olsson LE. Hyperpolarized ^{13}C MR angiography using trueFISP. Magn Reson Med. 2003; 50:256–62. DOI: 10.1002/mrm.10530 [PubMed: 12876701]
27. Laustsen C, Ostergaard JA, Lauritzen MH, Norregaard R, Bowen S, Sogaard LV, et al. Assessment of early diabetic renal changes with hyperpolarized [1-^{13}C]pyruvate. Diabetes Metab Res Rev. 2013; 29:125–9. DOI: 10.1002/dmrr [PubMed: 23166087]
28. Rider OJ, Tyler DJ. Clinical implications of cardiac hyperpolarized magnetic resonance imaging. J Cardiovasc Magn Reson. 2013; 15:93.doi: 10.1186/1532-429X-15-93 [PubMed: 24103786]
29. Coller HA. Is cancer a metabolic disease? Am J Pathol. 2014; 184:4–17. DOI: 10.1016/j.ajpath.2013.07.035 [PubMed: 24139946]
30. Keshari KR, Sriram R, Van Criekinge M, Wilson DM, Wang ZJ, Vigneron DB, et al. Metabolic reprogramming and validation of hyperpolarized ^{13}C lactate as a prostate cancer biomarker using a human prostate tissue slice culture bioreactor. Prostate. 2013; 73:1171–81. DOI: 10.1002/pros.22665 [PubMed: 23532911]
31. Zierhut ML, Yen YF, Chen AP, Bok R, Albers MJ, Zhang V, et al. Kinetic modeling of hyperpolarized $^{13}C_1$-pyruvate metabolism in normal rats and TRAMP mice. J Magn Reson. 2010; 202:85–92. DOI: 10.1016/j.jmr.2009.10.003 [PubMed: 19884027]
32. Swisher CL, Larson PEZ, Kruttwig K, Kerr AB, Hu S, Bok RA, et al. Quantitative measurement of cancer metabolism using stimulated echo hyperpolarized carbon-13 MRS. Magn Reson Med. 2014; 71:1–11. DOI: 10.1002/mrm.24634 [PubMed: 23412881]
33. Ward CS, Venkatesh HS, Chaumeil MM, Brandes AH, VanCriekinge M, Dafni H, et al. Noninvasive detection of target modulation following phosphatidylinositol 3-kinase inhibition using hyperpolarized ^{13}C magnetic resonance spectroscopy. Cancer Res. 2010; 70:1296–305. DOI: 10.1158/0008-5472.CAN-09-2251 [PubMed: 20145128]
34. Day SE, Kettunen MI, Gallagher FA, Hu D-E, Lerche M, Wolber J, et al. Detecting tumor response to treatment using hyperpolarized ^{13}C magnetic resonance imaging and spectroscopy. Nat Med. 2007; 13:1382–7. DOI: 10.1038/nm1650 [PubMed: 17965722]
35. Von Morze C, Larson PEZ, Hu S, Keshari K, Wilson DM, Ardenkjaer-Larsen JH, et al. Imaging of blood flow using hyperpolarized [^{13}C]urea in preclinical cancer models. J Magn Reson Imaging. 2011; 33:692–7. DOI: 10.1002/jmri.22484 [PubMed: 21563254]
36. Von Morze C, Larson PEZ, Hu S, Yoshihara HA, Bok RA, Goga A, et al. Investigating tumor perfusion and metabolism using multiple hyperpolarized ^{13}C compounds: HP001, pyruvate and urea. Magn Reson Imaging. 2012; 30:305–11. DOI: 10.1016/j.mri.2011.09.026 [PubMed: 22169407]

37. Von Morze C, Bok RA, Reed GD, Ardenkjaer-Larsen JH, Kurhanewicz J, Vigneron DB. Simultaneous Multiagent Hyperpolarized ^{13}C Perfusion Imaging. Magn Reson Med. 2014; 72:1599–606. DOI: 10.1002/mrm.25071 [PubMed: 24382698]
38. Lau AZ, Miller JJ, Robson MD, Tyler DJ. Cardiac perfusion imaging using hyperpolarized ^{13}C urea using flow sensitizing gradients. Magn Reson Med. 2015; doi: 10.1002/mrm.25713
39. Rose CJ, Mills SJ, O'Connor JPB, Buonaccorsi GA, Roberts C, Watson Y, et al. Quantifying spatial heterogeneity in dynamic contrast-enhanced MRI parameter maps. Magn Reson Med. 2009; 62:488–99. DOI: 10.1002/mrm.22003 [PubMed: 19466747]
40. Sanità P, Capulli M, Teti A, Galatioto GP, Vicentini C, Chiarugi P, et al. Tumor-stroma metabolic relationship based on lactate shuttle can sustain prostate cancer progression. BMC Cancer. 2014; 14:154.doi: 10.1186/1471-2407-14-154 [PubMed: 24597899]
41. Chen A, Kurhanewicz J, Bok R, Xu D, Joun D, Zhang V, et al. Feasibility of Using Hyperpolarized [1-^{13}C]Lactate as a Substrate for In Vivo Metabolic ^{13}C MRSI Studies. Magn Reson Imaging. 2009; 26:721–6. DOI: 10.1016/j.mri.2008.01.002.Feasibility
42. Hu S, Larson PEZ, VanCriekinge M, Leach AM, Park I, Leon C, et al. Rapid sequential injections of hyperpolarized [1-^{13}C]pyruvate in vivo using a sub-kelvin, multi-sample DNP polarizer. Magn Reson Imaging. 2013; 31:490–6. DOI: 10.1016/j.mri.2012.09.002 [PubMed: 23107275]
43. Hurwitz AA, Foster BA, Allison JP, Greenberg NM, Kwon ED. The TRAMP mouse as a model for prostate cancer. Curr Protoc Immunol. 2001; Chapter 20(Unit 20.5)doi: 10.1002/0471142735.im2005s45
44. Vargo-Gogola T, Rosen JM. Modelling breast cancer: one size does not fit all. Nat Rev Cancer. 2007; 7:659–72. DOI: 10.1038/nrc2193 [PubMed: 17721431]
45. Reed GD, von Morze C, Verkman AS, Koelsch BL, Chaumeil MM, Lustig M, et al. Imaging Renal Urea Handling in Rats at Millimeter Resolution using Hyperpolarized Magnetic Resonance Relaxometry. Tomography. 2016; 2:125–37. DOI: 10.18383/j.tom2016.00127 [PubMed: 27570835]
46. Schroeder MA, Atherton HJ, Ball DR, Cole Ma, Heather LC, Griffin JL, et al. Real-time assessment of Krebs cycle metabolism using hyperpolarized ^{13}C magnetic resonance spectroscopy. FASEB J. 2009; 23:2529–38. DOI: 10.1096/fj.09-129171 [PubMed: 19329759]
47. McGibney G, Smith M, Nichols S, Crawley A. Quantitative evaluation of several partial Fourier reconstruction algorithms used in MRI. Magn Reson Med. 1993; 30:51–9. DOI: 10.1002/mrm.1910300109 [PubMed: 8371675]
48. Volker, M. MRI Partial Fourier reconstruction with POCS. 2012. http://www.mathworks.com/matlabcentral/fileexchange/39350-mri-partial-fourier-reconstruction-with-pocs
49. Rosset A, Spadola L, Ratib O. OsiriX: An open-source software for navigating in multidimensional DICOM images. J Digit Imaging. 2004; 17:205–16. DOI: 10.1007/s10278-004-1014-6 [PubMed: 15534753]
50. Lustig M, Donoho D, Pauly JM. Sparse MRI: The application of compressed sensing for rapid MR imaging. Magn Reson Med. 2007; 58:1182–95. DOI: 10.1002/mrm.21391 [PubMed: 17969013]
51. Yen YF, Le Roux P, Mayer D, King R, Spielman D, Tropp J, et al. T_2 relaxation times of ^{13}C metabolites in a rat hepatocellular carcinoma model measured in vivo using ^{13}C-MRS of hyperpolarized [1-^{13}C]pyruvate. NMR Biomed. 2010; 23:414–23. DOI: 10.1002/nbm.1481 [PubMed: 20175135]
52. Yen, Y., Le Roux, P., Bok, R., Tropp, J., Chen, A., Zhang, V., et al. Apparent T_2 of ^{13}C-labeled Metabolites In Vivo. Proc. 16th Annu. Meet. ISMRM; Toronto, Canada. 2008. p. 1747
53. Chiavazza E, Kubala E, Gringeri CV, Düwel S, Durst M, Schulte RF, et al. Earth's magnetic field enabled scalar coupling relaxation of ^{13}C nuclei bound to fast-relaxing quadrupolar ^{14}N in amide groups. J Magn Reson. 2013; 227:35–8. DOI: 10.1016/j.jmr.2012.11.016 [PubMed: 23262330]
54. Palmer, AG, III. Protein NMR Spectrosc Princ Pract. Academic Press; 1996. Relaxation and dynamic processes.
55. Halestrap AP, Wilson MC. The monocarboxylate transporter family-Role and regulation. IUBMB Life. 2012; 64:109–19. DOI: 10.1002/iub.572 [PubMed: 22162139]

56. Juel C, Halestrap AP. Lactate transport in skeletal muscle - role and regulation of the monocarboxylate transporter. J Physiol. 1999; 517(Pt 3):633–42. DOI: 10.1177/088307389901400801 [PubMed: 10358105]
57. Halestrap AP. Monocarboxylic Acid Transport. Compr Physiol. 2013; 3:1611–43. DOI: 10.1002/cphy.c130008 [PubMed: 24265240]
58. Klahr, S., Mandel, LJ., Carolina, N. Handb Physiol Ren Physiol. Oxford University Press; 1992. Renal metabolism: integrated responses; p. 2263-333.
59. Malmqvist U, Arner A, Uvelius B. Lactate dehydrogenase activity and isoform distribution in normal and hypertrophic smooth muscle tissue from the rat. Pflugers Arch Eur J Physiol. 1991; 419:230–4. DOI: 10.1007/BF00371100 [PubMed: 1745598]
60. Keshari KR, Wilson DM. Chemistry and biochemistry of ^{13}C hyperpolarized magnetic resonance using dynamic nuclear polarization. Chem Soc Rev. 2014; 43:1627–59. DOI: 10.1039/c3cs60124b [PubMed: 24363044]
61. Rizi RR. A new direction for polarized carbon-13 MRI. Proc Natl Acad Sci U S A. 2009; 106:5453–4. [PubMed: 19336579]
62. Levy MN. Uptake of lactate and pyruvate by intact kidney of the dog. Am J Physiol. 1962; 202:302–8. [PubMed: 14464799]
63. Boyd LK, Mao X, Lu Y-J. The complexity of prostate cancer: genomic alterations and heterogeneity. Nat Rev Urol. 2012; 9:652–64. DOI: 10.1038/nrurol.2012.185 [PubMed: 23132303]
64. Kettunen MI, Hu D, Witney TH, Mclaughlin R, Gallagher FA, Bohndiek SE, et al. Magnetization Transfer Measurements of Exchange Between Hyperpolarized [1-^{13}C]Pyruvate and [1-^{13}C]Lactate in a Murine Lymphoma. Magn Reson Med. 2010; 63:872–80. DOI: 10.1002/mrm.22276 [PubMed: 20373388]
65. Yen, Y-F., Josan, S., Senadheera, L., Park, JM., Takahashi, A., Jang, T., et al. Non-CPMG Echo-Train Sequence for T_2 Mapping and Large SNR Gain in Hyperpolarized ^{13}C Imaging. Proc. 20th Annu. Meet. ISMRM; Melbourne, Aust. 2012. p. 4295
66. Hoskin PJ, Carnell DM, Taylor NJ, Smith RE, Stirling JJ, Daley FM, et al. Hypoxia in Prostate Cancer: Correlation of BOLD-MRI With Pimonidazole Immunohistochemistry-Initial Observations. Int J Radiat Oncol Biol Phys. 2007; 68:1065–71. DOI: 10.1016/j.ijrobp.2007.01.018 [PubMed: 17637389]
67. Martinez-Outschoorn UE, Pestell RG, Howell A, Tykocinski ML, Nagajyothi F, Machado FS, et al. Energy transfer in “parasitic” cancer metabolism: Mitochondria are the powerhouse and Achilles’ heel of tumor cells. Cell Cycle. 2011; 10:4208–16. DOI: 10.4161/cc.10.24.18487 [PubMed: 22033146]
68. Josan S, Park JM, Hurd R, Yen YF, Pfefferbaum A, Spielman D, et al. In vivo investigation of cardiac metabolism in the rat using MRS of hyperpolarized [1-^{13}C] and [2-^{13}C]pyruvate. NMR Biomed. 2013; 26:1680–7. DOI: 10.1002/nbm.3003 [PubMed: 23904148]
69. Josan S, Hurd R, Park JM, Yen YF, Watkins R, Pfefferbaum A, et al. Dynamic metabolic imaging of hyperpolarized [2-^{13}C]pyruvate using spiral chemical shift imaging with alternating spectral band excitation. Magn Reson Med. 2014; 71:2051–8. DOI: 10.1002/mrm.24871 [PubMed: 23878057]
70. Hu S, Yoshihara HAI, Bok R, Zhou J, Zhu M, Kurhanewicz J, et al. Use of hyperpolarized [1-^{13}C]pyruvate and [2-^{13}C]pyruvate to probe the effects of the anticancer agent dichloroacetate on mitochondrial metabolism in vivo in the normal rat. Magn Reson Imaging. 2012; 30:1367–72. DOI: 10.1016/j.mri.2012.05.012 [PubMed: 22819176]
71. Grant AK, Vinogradov E, Wang X, Lenkinski RE, Alsop DC. Perfusion imaging with a freely diffusible hyperpolarized contrast agent. Magn Reson Med. 2011; 66:746–55. DOI: 10.1002/mrm.22860 [PubMed: 21432901]
72. Shang H, Sukumar S, Von Morze C, Bok RA, Marco-Rius I, Kerr A, et al. Spectrally Selective Three-Dimensional Dynamic Balanced Steady-State Free Precession for Hyperpolarized C-13 Metabolic Imaging With Spectrally Selective Radiofrequency Pulses. Magn Reson Med. 2016; doi: 10.1002/mrm.26480

73. Weinreb J, Barentsz J, Choyke P, Cornud F, Haider M, Macura K, et al. PI-RADS v2 Prostate Imaging and Reporting and Data System: Version 2. Eur Urol. 2015; 69:16–40. DOI: 10.1016/j.eururo.2015.08.052 [PubMed: 26427566]
74. Fütterer JJ, Barentsz JO. 3T MRI of prostate cancer. Appl Radiol. 2009:25–32.
75. Li L, Wang L, Feng Z, Hu Z, Wang G, Yuan X, et al. Prostate cancer magnetic resonance imaging (MRI): multidisciplinary standpoint. Quant Imaging Med Surg. 2013; 3:100–12. DOI: 10.3978/j.issn.2223-4292.2013.03.03 [PubMed: 23630657]
76. Rosenkrantz AB, Neil J, Kong X, Melamed J, Babb JS, Taneja SS, et al. Prostate Cancer: Comparison of 3D T_2-Weighted With Conventional 2D T_2-Weighted Imaging for Image Quality and Tumor Detection. Am J Roentgenol. 2010; 194:446–52. DOI: 10.2214/AJR.09.3217 [PubMed: 20093608]
77. Nielsen PM, Hansen ESS, Nørlinger TS, Nørregaard R, Bertelsen LB, Jørgensen HS, et al. Renal Ischemia and Reperfusion Assessment With Three-Dimensional Hyperpolarized $^{13}C,^{15}N2$-Urea. Magn Reson Med. 2016; 76:1524–30. DOI: 10.1002/mrm.26377 [PubMed: 27548739]
78. Bertelsen LB, Nielsen PM, Qi H, Nørlinger TS, Zhang X, Stødkilde-jørgensen H, et al. Diabetes Induced Renal Urea Transport Alterations Assessed with 3D hyperpolarized $^{13}C,^{15}N$-Urea. Magn Reson Med. 2016; doi: 10.1002/mrm.26256
79. Hansen ESS, Stewart NJ, Wild JM, Stødkilde-jørgensen H, Laustsen C. Hyperpolarized $^{13}C,^{15}N_2$-Urea MRI for Assessment of the Urea Gradient in the Porcine Kidney. Magn Reson Med. 2016; 76:1895–9. DOI: 10.1002/mrm.26483 [PubMed: 27670826]
80. Otazo R, Candès E, Sodickson DK. Low-rank plus sparse matrix decomposition for accelerated dynamic MRI with separation of background and dynamic components. Magn Reson Med. 2015; 73:1125–36. DOI: 10.1002/mrm.25240 [PubMed: 24760724]
81. Shang, H., Larson, PEZ., Reed, G., Milshteyn, E., Von Morze, C., Ong, F., et al. Variable Flip Angle Design for Balanced SSFP Transient State Imaging to Improve HP ^{13}C MRI. Proc. 23rd Annu. Meet. ISMRM; Toronto, Canada. 2015. p. 3768
82. Otazo R, Kim D, Axel L, Sodickson DK. Combination of compressed sensing and parallel imaging for highly accelerated first-pass cardiac perfusion MRI. Magn Reson Med. 2010; 64:767–76. DOI: 10.1002/mrm.22463 [PubMed: 20535813]
83. Feng Y, Gordon JW, Shin PJ, von Morze C, Lustig M, Larson PEZ, et al. Development and testing of hyperpolarized ^{13}C MR calibrationless parallel imaging. J Magn Reson. 2016; 262:1–7. DOI: 10.1016/j.jmr.2015.10.018 [PubMed: 26679288]

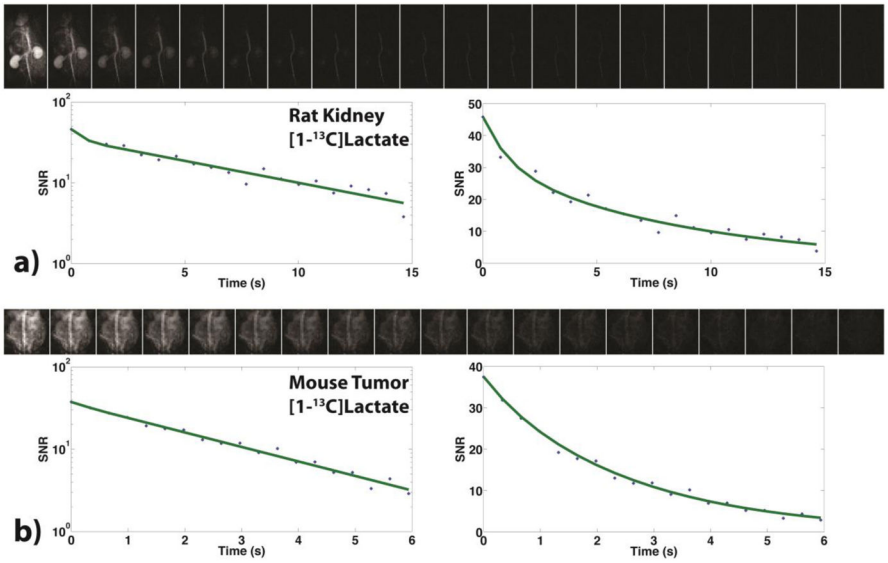

Figure 1.

Example of T_2 mapping acquisition and associated exponential decay with lactate. **a:** Full dynamic set of rat kidney images over the course of a T_2 mapping acquisition. A single pixel was chosen within the kidney that demonstrated a bilinear slope on the semilog plot on the left, which resulted in a biexponential decay, which can be seen in the plot on the right. **b:** Full dynamic set of mouse tumor images over the course of a T_2 mapping acquisition. A single pixel was chosen within the tumor that demonstrated a linear slope on the semilog plot on the left, which resulted in a monoexponential decay, as shown in the plot on the right.

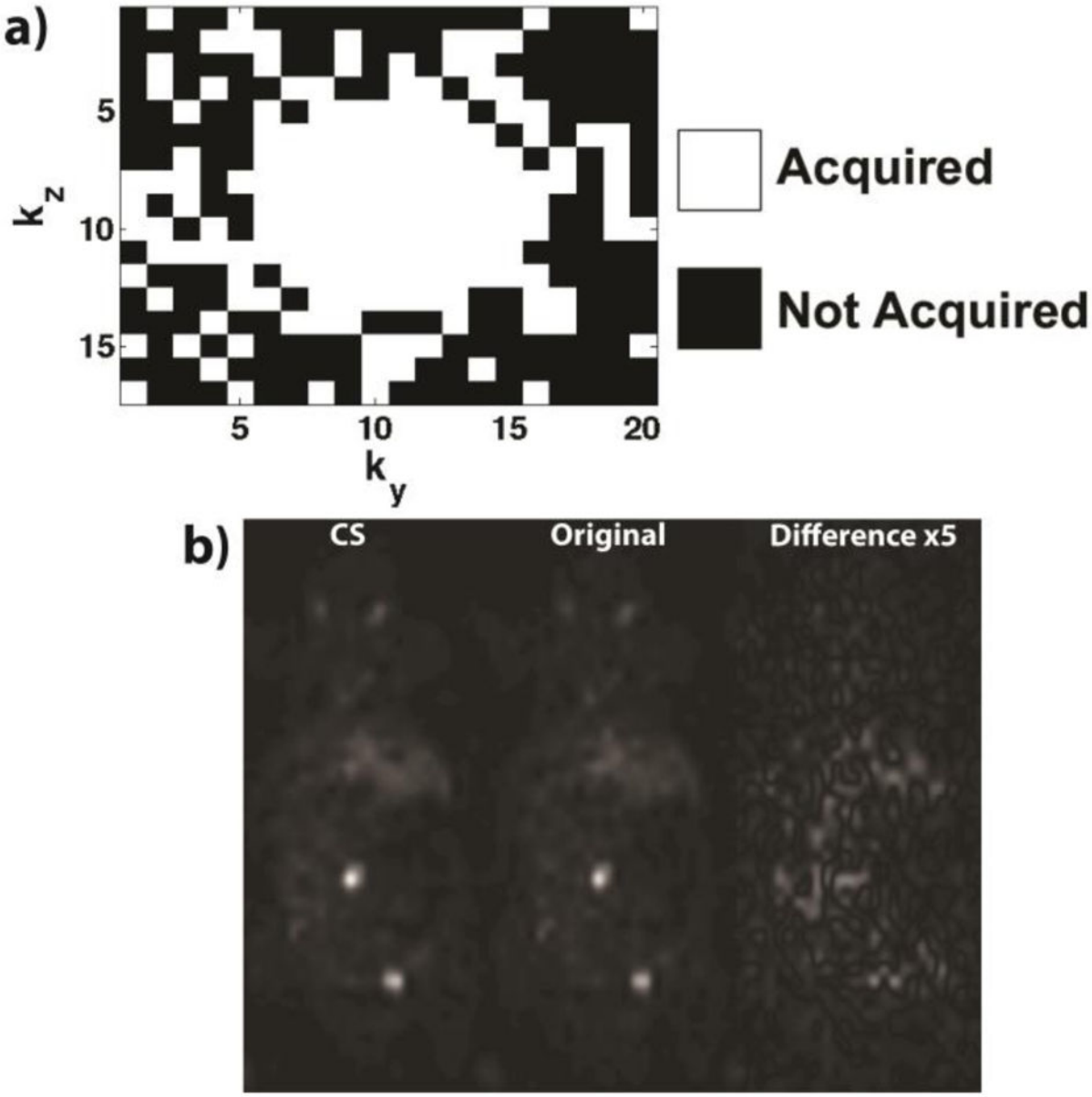

Figure 2.

Compressed sensing undersampling and retrospective simulations. **a:** A depiction of the variable-density pattern designed for dynamic imaging with compressed sensing. The pattern was designed using a Monte-Carlo simulation, as described previously in [50], such that only 50% of the phase encodes were acquired, and the center of k-space was fully sampled. **b:** A single slice comparison from a full 3D retrospective simulation of lactate in a TRAMP mouse with 50% undersampling. The reconstructed image agrees well with the original image as shown in the 5-fold amplified difference image, as well as having a SSIM of 0.9255 and a RMSE of 7.00%. The images have been zero-filled from 26 × 20 (matrix size in pattern shown in part a) to 256 × 256 for display purposes.

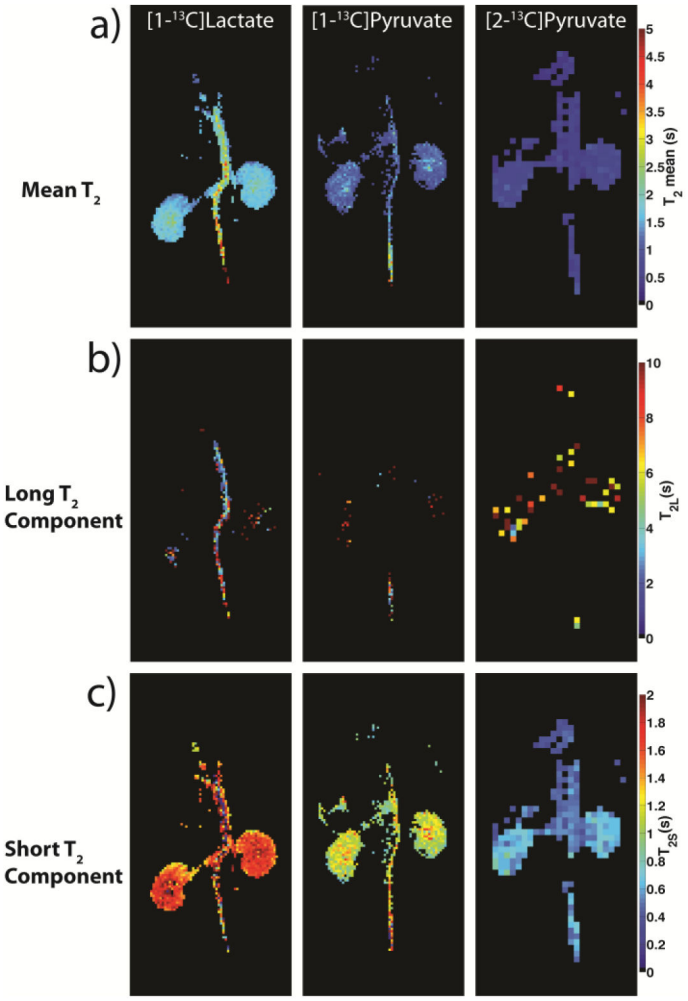

Figure 3.

T_2 mapping of normal rat kidneys and vasculature after injection of lactate, C_1-pyruvate, and C_2-pyruvate. **a:** The mean T_2 values (logarithmic mean of long and short components [45]) of each compound indicate lactate having the longest T_2 values among the three compounds with C_2-pyruvate having the lowest values. Each compound does exhibit the same trend of a T_2 decrease from the vasculature to the renal pelvis to the medulla, and ending with the cortex. **b:** The long (>2 s) T_2 components for each compound. **c:** The short (<2 s) T_2 components for each compound. The T_2 maps of C_1-pyruvate represent an aggregate T_2 of signals C_1-pyruvate and associated metabolic products. The images are displayed at 1 × 1 mm^2 for lactate and C_1-pyruvate, and 2.5 × 2.5 mm^2 for C_2-pyruvate.

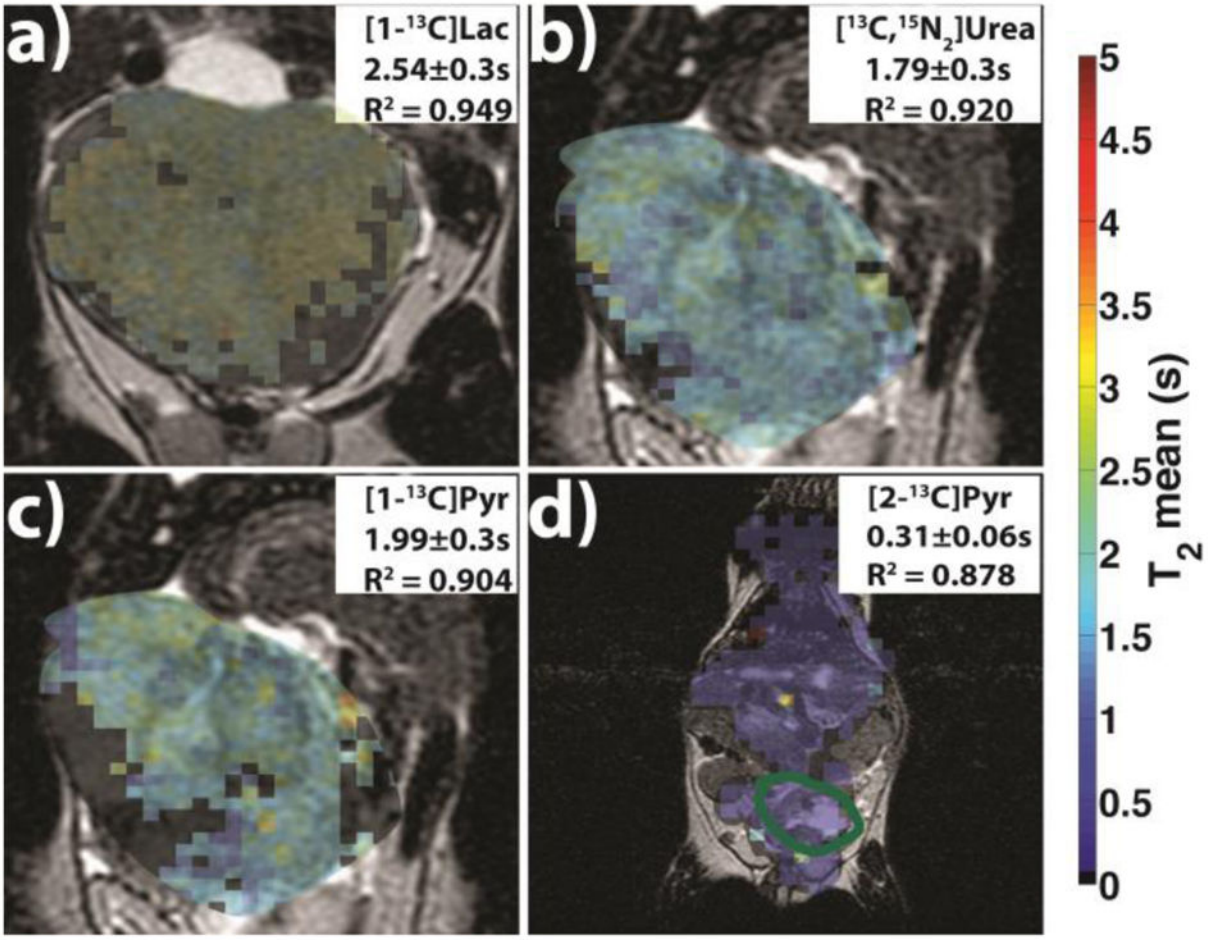

Figure 4.

Measured T_2 value maps from a transgenic prostate tumor overlaid on top of the ^1H image after injection of lactate (**a**), urea (**b**), C_1-pyruvate (**c**), and C_2-pyruvate (**d**). The tumor in panel **d** is outlined in green. Mean R^2 value of the depicted pixels is also displayed, with black pixels excluded from the calculation. The images are displayed at 1×1 mm^2 for urea, lactate and C_1-pyruvate, and 2×2 mm^2 for C_2-pyruvate.

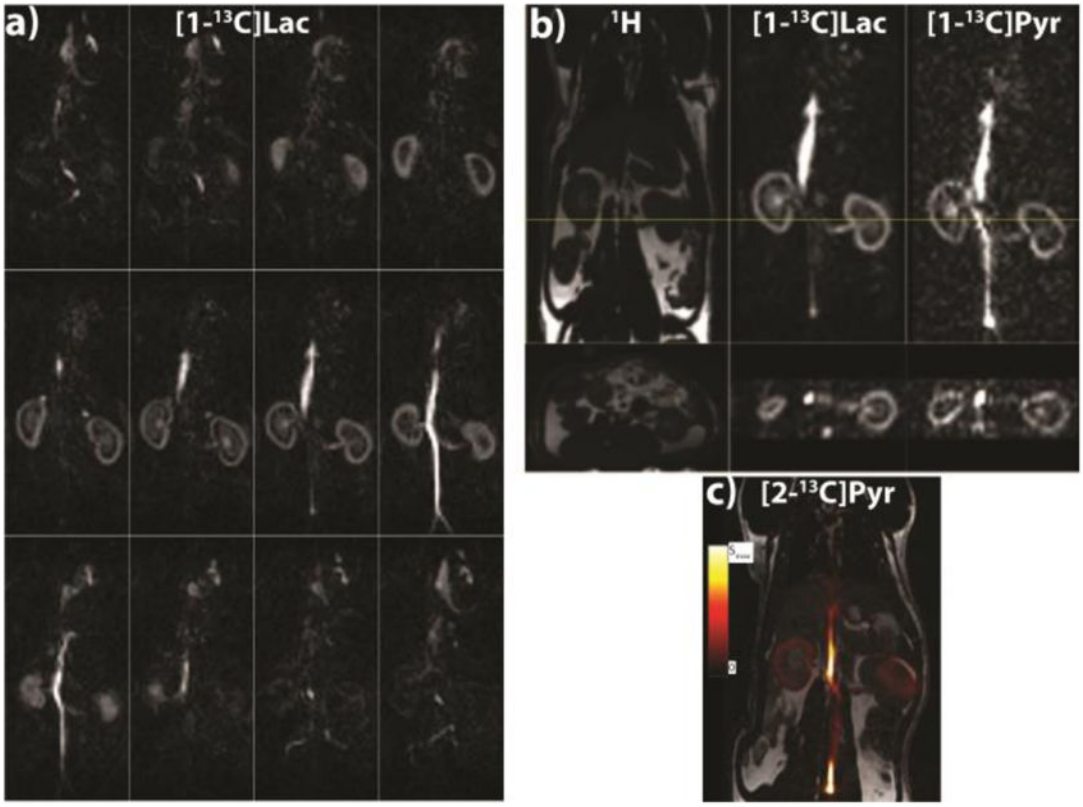

Figure 5.

High resolution 3D 1.5 mm isotropic imaging of lactate, C_1-pyruvate, and C_2-pyruvate. **a:** All 12 slices in a 3D lactate acquisition are shown here. Uptake of lactate can be seen within the kidneys, vasculature, and the heart. **b:** A representative coronal and axial slice (B) from the 3D lactate and C_1-pyruvate acquisitions are shown next to an anatomical ^1H image. The coronal and axial reformats (yellow line indicates axial slice position) show hyperintense signal from the vasculature and renal pelvis. The lactate acquisition exhibited higher SNR compared to the C_1-pyruvate. **c:** A representative coronal slice from a 3D C_2-pyruvate acquisition overlaid atop the anatomical ^1H image. The C_2-pyruvate acquisition had considerably less SNR compared to lactate or C_1-pyruvate, but uptake within the vasculature and kidneys is still visible. The images were zero-filled to 256 × 256 for display purposes.

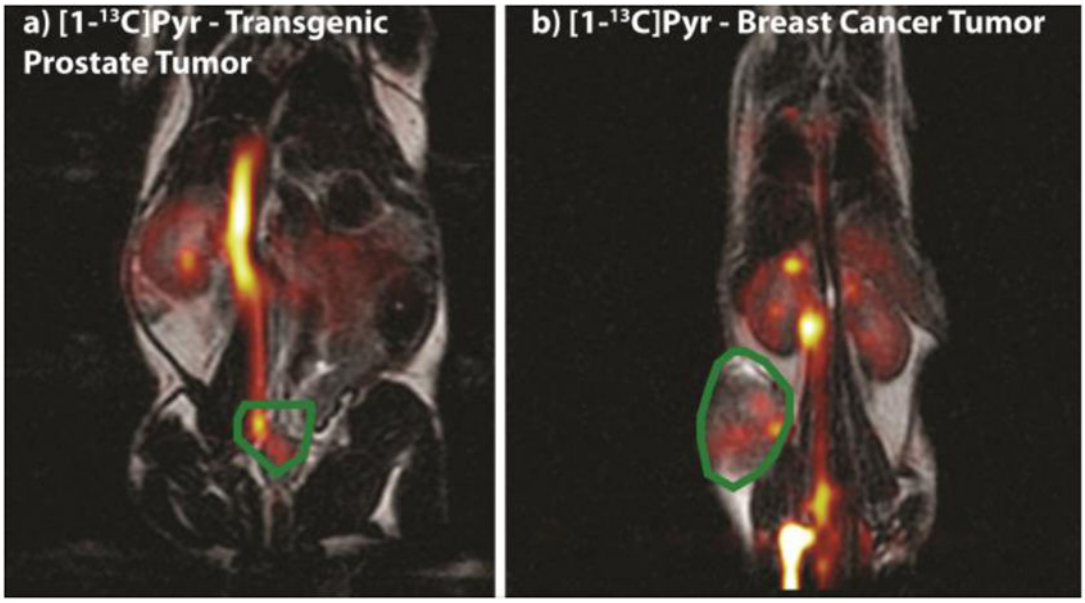

Figure 6.

3D images overlaid on ^{1}H anatomical images of C_1-pyruvate in transgenic prostate tumor (**a**) and breast cancer mouse (**b**). The blue ROIs indicate tumor region. Uptake of C_1-pyruvate can be seen in vasculature, kidneys, and tumor, with resolution high enough to see uptake in the renal cortex and renal pelvis, which is similar as rat kidney imaging. The images were zero-filled from 32 × 24 (2 × 2 mm^2 in-plane resolution) to 256 × 256 for display purposes.

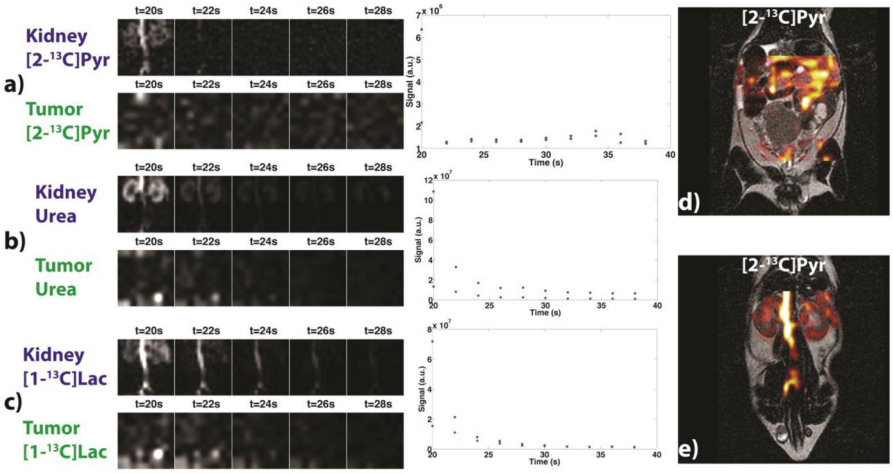

Figure 7.

Dynamic imaging of a transgenic prostate tumor with C_2-pyruvate, urea, and lactate. **a–c:** First five time-points of a representative kidney and tumor slice from the 3D dynamic imaging of C_2-pyruvate (a), urea(b) and lactate (c) are shown here, with associated decay curves for each slice. **d and e:** Carbon images within the tumor (and surrounding tissue) (d) and kidneys (e) overlaid on the anatomic ^{1}H image are also presented. The kidney slice has strong uptake of all three compounds, while the tumor shows varied uptake, with a clear distinction in decay curves between the healthy kidney tissue and diseased tumor tissue. The images were zero-filled to 256 × 256 for display purposes.

Table 1

Anatomical Distribution of Mean T_2 within Rat Kidney and Vasculature

	Lactate	C_1-Pyruvate	C_2-Pyruvate
Renal Pelvis	2.21±0.39 s	1.36±0.09 s	
Medulla	1.95±0.24 s	1.26±0.17 s	0.73±0.07 s
Renal Cortex	1.70±0.14 s	1.16±0.14 s	
Vasculature	2.58±0.33 s	1.38±0.08 s	0.75±0.19 s
R^2	0.938	0.943	0.877

The mean T_2 values (mean and standard deviation of all three rats) and associated standard deviations within different regions of the rat kidney and vasculature for all three compounds are presented here and demonstrate the longest T_2 values exist in the vasculature, while within the kidney there is a decrease from the renal pelvis to the medulla to the renal cortex, with all components long enough to exploit in 3D imaging. The resolution of the C_2-pyruvate T_2 mapping was not high enough to distinguish the different regions of the kidneys. Mean R^2 values of depicted pixels in Figure 3 are presented here, with black pixels excluded from calculation.

Table 2

Anatomical Distribution of SNR within Rat Kidney and Vasculature

	Lactate	C_1-Pyruvate	C_2-Pyruvate
Renal Pelvis	56.7±9.1	31.3±15.9	
Medulla	28.8±6.1	15.7±6.1	10.2±5.2
Renal Cortex	53.1±14.4	25.4±8.3	
Vasculature	129±19.8	96.5±14.9	34.5±17.8

The mean SNR values and associated standard deviation within different regions of the rat kidney and vasculature for all three compounds are presented here. The highest SNR values were seen in the vasculature, while within the kidney there is a decrease from the renal pelvis to the renal cortex to the medulla. The SNR was high enough, however, to distinguish these regions for lactate and C_1-pyruvate, and visualize overall kidney biodistribution for C_2-pyruvate.